

Various Solvent-Binder Compositions and their Crystalline Phase for Optimal Screen-Printing of NMC Cathodes

Rafal Sliz,^{*[a]} Ivy Saha Roy,^[a] Palanivel Molaiyan,^[b] Juho Välikangas,^[b] Tero Jakkila,^[a] Mika Christophliemk,^[b] Tao Hu,^[b] Hai Harry Nguyen,^[a] Esa Hannila,^[a] Sofia Ilikainen,^[a] Ulla Lassi,^[b] and Tapio Fabritius^[a]

This research examines the compatibility and performance of various solvents and binders in the battery cathode fabrication. The study focused on the applicability of solvents, including DMF, NMP, p-Xylene, Ethanol, Toluene, Cyrene, and KJCPMA, in conjunction with binders such as PVDF #9300, PVDF #1100, HSV 1810, PVP, Opanol N150, and Opanol B15 for NMC-based slurry formulation. Each solvent-binder combination was evaluated with NMC material, and those demonstrating optimal solubility, adhesion, and film quality were selected for cathode screen-printing trials. Results show that the combination of NMP solvent and HSV 1810 binder outperformed other pairings

in cycling stability and capacity retention, achieving 87% capacity retention after 1,000 1C/1C cycles. Comprehensive analyses using SEM, XRD, and FTIR offered insights into the structural and binder phase characteristics of the fabricated cathodes, especially the alterations in binder crystallinity phases (α , β , and γ). The data suggest that the use of the homopolymer HSV 1810, irrespective of the solvent, results in a pronounced presence of the γ -phase within the binder, which subsequently improves battery performance. Moreover, the findings underscore the importance of the solvent-binder combinations in enhancing battery performance and longevity.

Introduction

Regardless of application, batteries are ubiquitous. Currently there are three main drivers of the battery development: more capable portable consumer electronic devices and IoT, popularization of electric vehicles (EVs), and need for large-scale energy storage systems to support smart grid and energy supplied by discontinuous (irregular) renewable energy sources (wind & solar). Batteries can be divided into two types: primary (non-rechargeable) and secondary (with charge-recharge capability). Among secondary batteries, the most common are the batteries that rely on transfer of the ions between cathode and anode. Currently, lithium-ion (Li-ion) batteries are the most popular but thanks to technological advances, new concepts are emerging; i.e., sodium-ion or magnesium-ion batteries.^[1]

In Li-ion batteries, to ensure appropriate ion transfer, the electrodes are immersed in a liquid electrolyte and physically separated by a separator.^[2] To improve the performance and safety, many researchers concentrate their efforts on replacing

liquid electrolyte with its solid-state alternative.^[3,4] However, most solid-state electrolytes suffer from poor ionic conductivities at room temperatures and stability issues. In general, Li-ion technology offers relatively high performance, but there is a continuous demand for more capable, smaller, safer, and more environmentally friendly batteries.

The essential aspects in regard to environmental friendliness are related to utilization of raw materials, usage of toxic and harmful production materials, energy efficiency of production, and application of appropriate fabrication methods.^[5] To make the batteries more sustainable, all these concerns should be addressed, without compromising battery's performance.

The typical cathode of a Li-ion battery is composed of three materials: active material, binder, and conductive additives (Figure 1a).

The first component of a Li-ion battery's cathode, the active material, serves as the host for lithium ions, facilitating the storage and release of energy during charge and discharge cycles. It also contributes to the battery's conductivity, aiding efficient energy transfer. Common cathode materials include layered oxides like lithium cobalt oxide, lithium manganese oxide, lithium nickel manganese cobalt oxide, lithium nickel aluminum oxide, and lithium iron phosphate, chosen based on their performance traits and the specific battery application.^[6–9] The choice of active material significantly impacts the battery's voltage, which is determined by the electrochemical potential difference between the cathode and anode, while the amount of active material directly influences the battery's capacity. It is essential for the active material to be stable under varying operating conditions for the battery's longevity and safety.

[a] Prof. R. Sliz, I. S. Roy, T. Jakkila, H. H. Nguyen, Dr. E. Hannila, S. Ilikainen, Prof. T. Fabritius
Optoelectronics and Measurement Techniques Unit, University of Oulu
90570 Oulu, Finland
E-mail: rafal.sliz@oulu.fi

[b] Dr. P. Molaiyan, J. Välikangas, M. Christophliemk, Prof. T. Hu, Prof. U. Lassi
Sustainable Chemistry Research Unit, University of Oulu
90570 Oulu, Finland

 Supporting information for this article is available on the WWW under
<https://doi.org/10.1002/batt.202300527>

 © 2024 The Authors. *Batteries & Supercaps* published by Wiley-VCH GmbH.
This is an open access article under the terms of the Creative Commons Attribution License, which permits use, distribution and reproduction in any medium, provided the original work is properly cited.

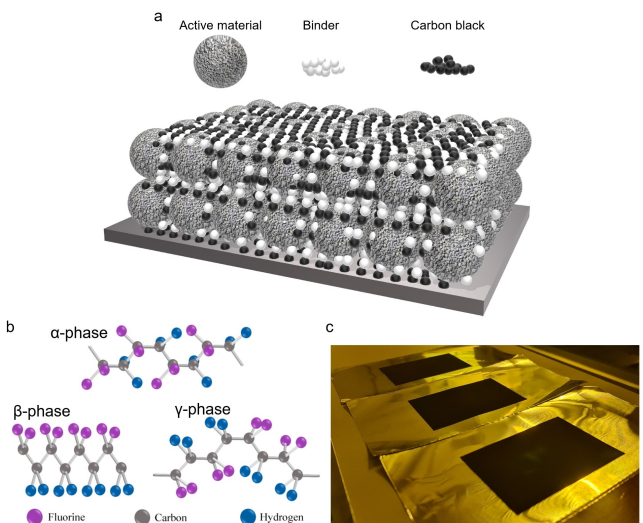


Figure 1. a) Composition of cathode composed of active material (NMC), binder, and conductive additive (Carbon C45), b) Various phases of PVDF binder utilized in battery fabrication, c) Screen-printed cathodes.

The second component of cathodes, the conductive additives, are mostly based on carbon black, a form of paracrystalline carbon material with high surface-area-to-volume-ratio that serves as electrical conductivity enhancer within the cathode layer.^[10] In order to increase the conductivity within the cathode layer and the rate capability, other dopants can be also used, such as carbon nanotubes or graphene.^[11–13] The third component of lithium-ion battery's cathode, binders, are essential for maintaining the mechanical stability of the electrode structure by ensuring the active material particles are securely adhered to the current collector. They play a significant role in supporting an uninterrupted conductive network which ensures efficient electron movement and optimal utilization of active material particles. In addition, they modulate ionic conductivity within the electrode, impacting the mobility of lithium ions during the charge and discharge processes. They also contribute to the management of volumetric changes in active materials during these processes, preventing the electrode from disintegration. Moreover, their chemical stability is crucial for preventing undesirable reactions with the electrolyte or active materials, thereby enhancing the battery's performance and lifespan. The selection of the right binder is, therefore, a crucial aspect in advancing lithium-ion battery technology.

The manufacture of Li-ion batteries utilizes a variety of binders, each possessing distinct properties, advantages, and disadvantages. Styrene-butadiene rubber is frequently used in conjunction with carboxymethyl cellulose (CMC) in battery electrodes.^[14] This pairing is water-soluble, offering a more environmentally friendly alternative to some other options. CMC, a water-soluble cellulose derivative, is another prevalent binder. In addition to its environmental benefits, it offers excellent film-forming properties. Polyacrylic acid has gained attention as another promising alternative due to its strong

adhesion capabilities and electrochemical stability, making it particularly well-suited for silicon-based anodes where it effectively manages large volume changes.^[15] Sodium alginate, a natural polymer derived from brown algae, is also employed as a binder in lithium-ion and sodium-ion batteries.^[16,17] Another considerable alternative is Opanol, a brand name for a specific type of polyisobutylene, which is a synthetic rubber or elastomer. Renowned for its exceptional chemical stability, gas impermeability, and resistance to weathering, ozone, and UV radiation, Opanol is frequently utilized in the production of sealants, adhesives, and lubricants, as well as for modifying other materials to improve their properties. Given its distinctive characteristics, Opanol emerges as a promising option for use as a binder in battery applications.^[18,19]

However, despite these varied options, polyvinylidene fluoride (PVDF) remains the most common binder in lithium-ion batteries due to its excellent adhesive properties and chemical resistance.^[20,21] PVDF, a semi-crystalline polymer, exists in five distinct phases: α , β , γ , δ , and ϵ (Figure 1b).^[22] Among these, the α phase is nonpolar, whereas the β , γ , and δ phases exhibit macroscopic polarization due to their specific chain conformations. The β and γ phases, in particular, have been the subject of extensive study due to their high spontaneous polarization values.^[23]

The electroactive β -phase of PVDF has been reported to be induced by electrical poling and stretching of the polymer at high temperatures. Methods such as the selection of PVDF copolymers, solution casting of pristine PVDF, and incorporation of nanofillers have proven successful in promoting the electroactive (β and γ) phases of PVDF.^[24–26]

Interestingly, PVDF films that exhibit the γ phase and possess a dense microstructure have been observed to perform well in energy storage applications compared to other variations, underscoring the influence of phase and structure on the material's performance.^[27–29] Song et al. demonstrated higher performance in LFP cells with an increased β phase.^[30] Concurrently, Loghavi et al. indicated that for NCA batteries, the β -phase offers better electrochemical and mechanical performance.^[31] In the context of NMC cathode chemistry, Ren et al. doped PVDF with ionic salts to alter its phase, observing improved battery performance in samples with a higher β -phase.^[32] From the perspective of using PVDF as separator membranes, Kundu et al. demonstrated enhanced battery performance with increased β -phase content.^[33] Additionally, Lizundia et al. showed that doping PVDF with cellulose nanocrystals resulted in an elevated electroactive γ -phase of PVDF, offering a promising material blend for various applications.^[34] Simultaneously, Luo et al. showed that β -phase PVDF at Cu anode current collectors enhances the performance of LFP batteries.^[35]

However, it is important to note that its environmental impact, cost, and limited selection of compatible solvents have spurred interest in various alternatives. One of the alternatives is a functional homopolymer of vinylidene fluoride – Arkema Kynar HSV 1810. This material was designed to be used as a cathode binder in lithium-ion batteries. According to the producer, HSV 1810 is a high-performance binder that offers

excellent electrical conductivity, thermal stability, and chemical resistance. At the same time, HSV 1810 is highly processable, making it easy to formulate various inks.

The three aforementioned materials (active, binder, and conductive additive) are mixed together with a solvent to form a slurry that is further deposited on the surface of current collector, usually aluminum. Currently the most common solvent used in cathode production is N-Methyl-2-Pyrrolidone (NMP) – a polar aprotic solvent widely used in chemical processing in various industries with properties highlighted in Table 1. It is highly miscible with most organic solvents, chemically and thermally stable, and has high boiling and flash points. However, NMP is toxic, and its processing and recovery requires extensive amount of energy. At the same time, the usage of NMP is becoming prohibited in the increasing number of countries.^[36] Therefore, many researchers seek for green alternatives to replace NMP.^[37,38]

Some of the efforts involve introduction of complementary solvents, such as DMSO (Dimethylsulfoxide), Cyrene (Dihydrole-voglucosenone), or γ -Valerolactone. These solvents offer similar dissolving properties as NMP, but the formulated cathode slurries have relatively high boiling point (more energy needed for cathode drying), insert undesired sulfur impurities (DMSO), and provide cathode layers with poorer adhesion (Cyrene, or γ -Valerolactone), resulting in lower battery performance.^[39] Although Dimethylformamide (DMF) offers more suitable properties than NMP (lower boiling point, lower viscosity and surface tension, and higher autoignition temperature) for cathode slurries, its wide usage is questionable due restrictions related to toxicity – added to the Registration, Evaluation and Authorization of Chemicals (REACH) list, restricting its usage in consumer applications.^[36]

Water is another environmentally friendly solvent to formulate cathode slurries and many researchers are exploring utilization of water in cathode fabrication. The usage of water also beneficial in terms of reduction of energy consumption during drying due to lower boiling point than conventional solvents.^[40] However, water does not dissolve PVDF and negatively influence the performance of the cathodes, especially those with high nickel content.^[41,42]

KJCPMA (3-methoxy-N,N-dimethylpropanamide) emerges as a promising alternative to the increasingly restricted NMP. This highly amphiphilic amide solvent offers a reduced toxicity

profile.^[43] Notably, KJCPMA possesses the ability to dissolve a diverse range of materials, spanning various polarity levels. Its favorable properties make it particularly suitable for formulating a wide array of inks and slurries, as detailed in Table 1. Another alternative for cathode production is dry processing, where the materials are mixed in a dry form, without using any solvents, and then deposited on the surface of current collector.^[44] Although this very promising approach resolves many issues related to usage of solvents and high energy consumption during solvents drying/recovery, the current dry-process is very challenging and fabricated cathodes do not offer the satisfactory performance, especially at high C-rates.^[45]

Another aspect of sustainability is related to cathode fabrication technologies. Slot-die coating, the predominant industrial method of coating batteries' electrodes, falls under a group of techniques where the slurry is channeled through a slot opening onto a mobile current collector. This method, while specifically intended for producing evenly thin films on flat surfaces at high production rates, is not adaptable to more intricate multilayer battery designs or different shapes, unlike some printing techniques (Figure 1c).

Printing technologies, such as spray printing or screen printing, have several distinct advantages over slot-die coating for battery fabrication.^[46–48] Firstly, they are exceptionally versatile, capable of handling complex multilayer battery architectures and different shapes that slot-die coating struggles with.^[49] This flexibility is critical in modern battery designs where structural complexity is often needed. Secondly, printing techniques have the potential to decrease material waste by accurately depositing the precise amount of slurry required, enhancing the overall manufacturing efficiency.^[50]

This work focuses on analysis of applicability of various solvents (DMF, NMP, p-Xylene, Ethanol, Toluene, Cyrene, and KJCPMA) combined with different binders (PVDF#9300, PVDF#1100, HSV 1810, PVP, Opanol N150, and Opanol B15) for NMC-based slurry formulation, screen printing-compatibility, cathode film formation and adhesion, and overall battery performance. Importantly, some of the investigated binders were incompatible with the used solvents due to poor solvability, polarity, film quality, and surface adhesion. Therefore, the further investigations concentrated on compositions that offer promising results in terms of film quality and surface adhesion to current collectors. The physicochemical methods and post-mortem analyses were applied to explain the behavior of the batteries with applied various solvent-binder compositions.

Results and Discussion

The prescreening results depicted in Figure 2 illustrate the behavior of various solvents and binders. While Opanol-based binders display reasonable solvency in p-Xylene and Toluene, the respective NMC layers offered unsatisfactory adhesion to the aluminum current collector. A potential reason for this behavior is the polarity of the solvents. The non-polar solvents

Table 1. Properties of the solvents used in this research.

Solvent	Surface tension [mN/m at 25 °C]	Viscosity [mPa s]	Boiling point [°C]	Autoignition temperature [°C]
DMF	37	0.92	155	445
NMP	41	1.66	202	252
p-Xylene	29	0.65	138	528
Ethanol	22	1.07	78	365
Toluene	28	0.56	110	480
Cyrene	72	14.5	226	296
KJCPMA	29	2.3	215	NA



Figure 2. Matrix representing various solvent-binder compositions. Adhesion and film quality were analyzed using tape test and visual inspection.

(p-Xylene, Toluene) dissolve the Oppanol-based binders while polar solvents (NMP, DMF, KJCPMA, and Cyrene) show better compatibility with PVDF-based binders. Although ethanol is a

polar solvent, it is not compatible with either type of the binders.

The PVDF-based and HSV 1810-based binders exhibit the highest compatibility with DMF, NMP, and KJCPMA – Figure 3 demonstrates an excellent solubility of the selected solvent-binder compositions.

Figure 4 and Table 2 demonstrate the results of the rheological analysis of NMC slurries based on the selected solvent-binder mixes. The contact angle data suggest that the PVDF-based slurries demonstrate lower contact angles, compared to their HSV 1810-based equivalents. Interestingly, in terms of contact angle, the behavior of the slurries contrasts with that of the pure solvents. Considering the surface tension values of the pure solvents – NMP (38.6 mN/m), DMF (35.5 mN/m), and KJCPMA (34.2 mN/m), it is unexpected that the slurries with KJCPMA exhibit the highest contact angle, followed by those with DMF, and then NMP. This behavior can be partially explained by the difference in the viscosity of the formulated slurries (Table 2) and their respective pure solvents (Table 1). The HSV 1810-based slurries are less significantly affected by the drop flattening phenomena. Another aspect involves the disparity in molecular weights and melt viscosities of the binders used. The used PVDF has a molecular weight of 2.8×10^5 and a melt viscosity of 33 kP. In contrast, HSV 1810 exhibits a molecular weight of 7×10^5 and a melt viscosity ranging between 70 and 75 kP. Moreover, the densities of these binders are notably similar, each being approximately 1.78 g/cm³.

Post-printing of the chosen solvent-binder compositions, the films were characterized with the SEM (Figure 5 & 6) and optical profilometry (Figure S6). Figure 5 displays the cross-sectional images of the cathode films, revealing that all layers have a similar thickness of approximately 55 µm, and similar roughness ($S_q 3.89 \pm 1.11 \mu\text{m}$) (Table S2). Figure 6 displays the surfaces of the samples. For those utilizing HSV 1810, the

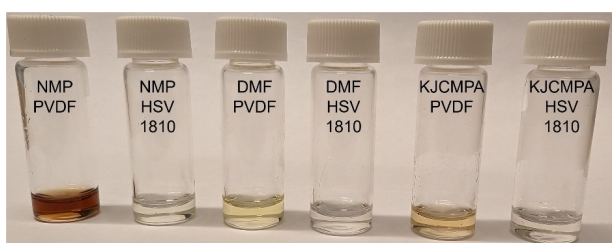


Figure 3. Selected solvent-binder compositions demonstrating excellent solubility.

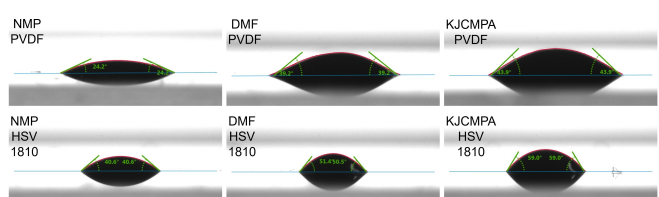


Figure 4. Contact angle of the selected solvent-binder mixes.

Table 2. Rheological properties of the formulated NMC slurries.

Solvent	Binder	Contact Angle [°]	Viscosity [mPa s]
NMP	PVDF	24.2	700
NMP	HSV 1810	40.6	17,000
DMF	PVDF	39.2	630
DMF	HSV 1810	51.4	17,000
KJCPMA	PVDF	43.9	6,500
KJCPMA	HSV 1810	59.0	40,000

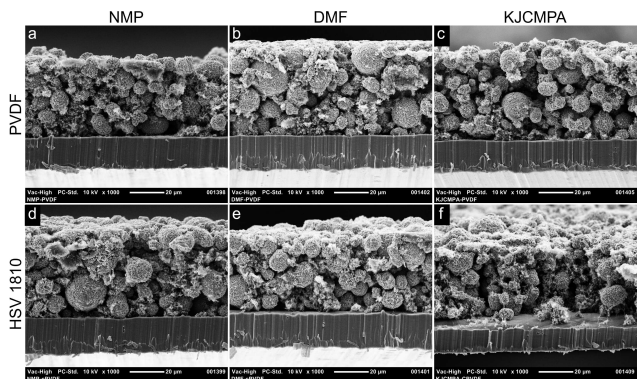


Figure 5. Cross-sectional SEM images of NMC cathodes printed with various solvent-binder compositions, a) NMP-PVDF, b) DMF-PVDF, c) KJCMPA-PVDF, d) NMP-HSV 1810, e) DMF-HSV 1810, f) KJCMPA-HSV 1810.

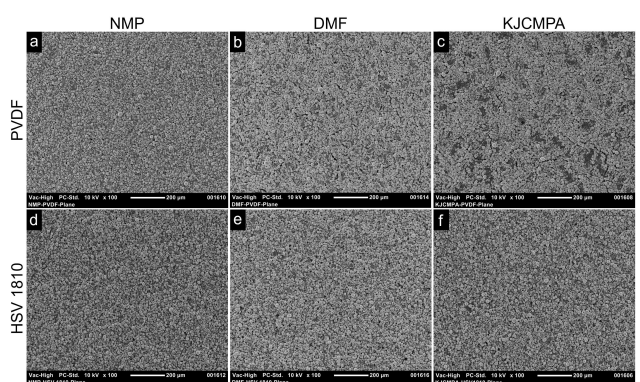


Figure 6. SEM images in plain view of NMC cathodes printed with various solvent-binder compositions, a) NMP-PVDF, b) DMF-PVDF, c) KJCMPA-PVDF, d) NMP-HSV 1810, e) DMF-HSV 1810, f) KJCMPA-HSV 1810.

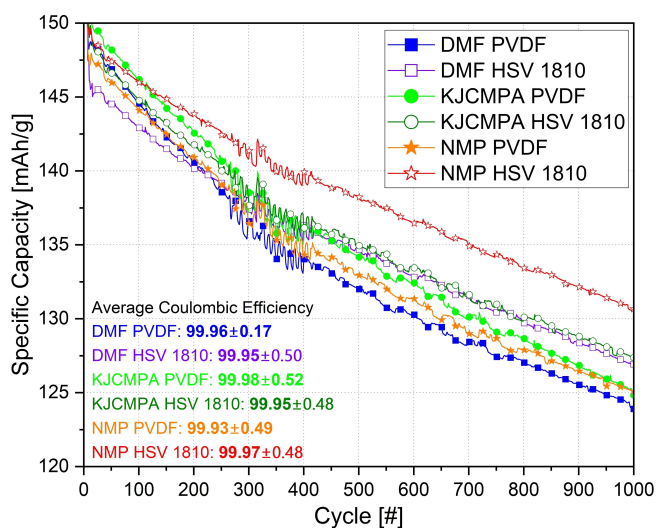


Figure 7. Discharge capacity of pouch cell batteries cycled 1,000 times at a 1C/1C rate. The instability of the specific capacity between cycles 250 and 400 is related to air conditioning system malfunctioning and temperature changes.

surface appearance is consistent. In contrast, PVDF-based samples exhibit varying characteristics: the NMP-based sample

is uniform, the DMF-based sample reveals minor cracks, and the KJCMPA-based sample exhibits significant cracks and inconsistencies.

Following the printing process, the cathodes were used to assemble coin (half-cell) and pouch cells. Figure 7 shows the results of cycling (1C/1C) for pouch cells with the selected cathodes. Regardless of the solvent used to dissolve the binder, batteries using HSV 1810 as a binder exhibit the best cycling performance. While KJCMPA and DMF mixed with HSV 1810 show similar performance, the NMP HSV 1810 demonstrated outstanding performance compared to any other tested device. Additionally, a set of extra cells, which provided information about variation (as detailed in the supporting information – Figure S1), also highlighted the exceptional performance of the NMP HSV 1810 composition. The high (> 99.9%) average coulombic efficiency suggests low energy losses during charging and discharging for all samples used in this research.

Table 3 presents the capacity fading in batteries based on various solvent-binder compositions. After 1,000 cycles, NMP HSV 1810 offers 87% capacity retention. Although the advantages of HSV 1810 are the most visible for NMP solvent, the remaining mixtures result in batteries that show higher performance with HSV 1810 than with PVDF.

The C-rate analysis in Figure 8 indicates that the charging process is nearly identical across all samples, regardless of the solvent-binder composition. For discharge at 0.1 C only DMF PVDF offers a slightly lower specific capacity (~166 mAh/g) than the other solvent-binder compositions (~170 mAh/g). For discharge at 1 C rate, the specific capacity of all samples decreases to approximately 155 mAh/g and the DMF PDVF demonstrates the worst performance. For 2C discharge, the specific capacity decreases to 144 mAh/g for most of the samples, while DMF PVDF sample demonstrates a capacity of 136 mAh/g.

Figure 9 presents the electrochemical impedance spectroscopy results of the tested pouch cells. Low R_s suggests that all electrodes are in good contact with the electrolyte and the binder or solvent does not significantly affect this parameter. The variation in R_{SEI} resistance indicates that battery systems with HSV 1810 binder create interfaces R_{SEI} of higher resistance.

Table 3. Discharge capacity fading of pouch cells after 1,000 1 C/1C cycles.

Solvent	Binder	Initial capacity [mAh/g]	Capacity after 1,000 cycles [mAh/g]	Capacity retained [%]
NMP	PVDF	148	124	83.8
NMP	HSV 1810	149	130	87.2
DMF	PVDF	149	124	83.2
DMF	HSV 1810	147	126	85.7
KJCMPA	PVDF	150	124	82.7
KJCMPA	HSV 1810	151	126	83.4

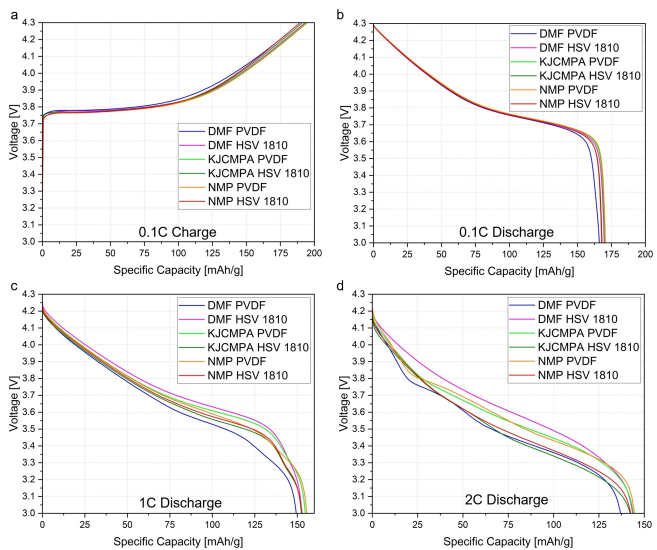


Figure 8. Results of C-rate testing of batteries with various solvent-binder compositions, a) 0.1C charge, b) 0.1C discharge, c) 1C discharge, d) 2C discharge.

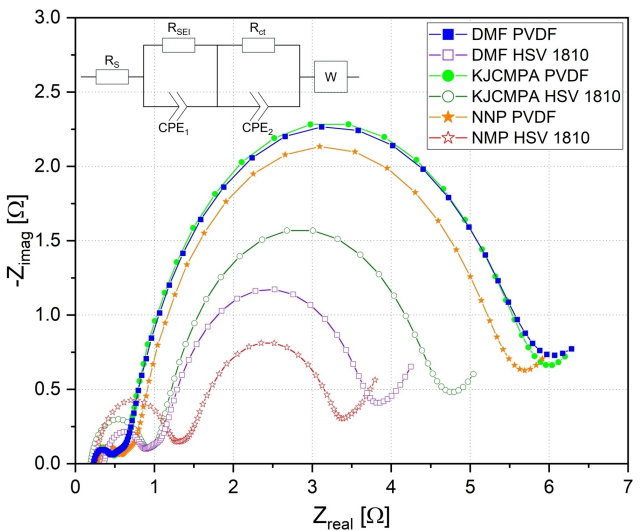


Figure 9. Electrochemical impedance spectroscopy of batteries with various solvents after 1,000 cycles.

At the same time, variation in R_{ct} differentiates significantly between PVDF and HSV 1810 samples – for all HSV 1810 samples, the R_{ct} values are smaller, especially for NMP HSV 1810, suggesting more efficient electron transfer for HSV 1810 samples than for PVDF. The values are consistent with those previously published for NMC batteries.^[51–53] Detailed results of modeling are provided in the supporting information (Table S1).

Table 4 displays the sheet resistance and conductivity of the printed NMC cathodes with different solvent-binder compositions. The HSV 1810 compositions show increased conductivity regardless of the solvent. Also, NMP HSV 1810 composition offers the highest conductivity (26.65 S/m) among all the samples. For PVDF-based compositions, NMP shows the best

Table 4. Conductivity of the printed NMC cathodes.

Solvent	Binder	Sheet resistance [ohm m]	Conductivity [S/m]
NMP	PVDF	1254 ± 0.12	17.72 ± 0.001
NMP	HSV 1810	683 ± 0.04	26.65 ± 0.001
DMF	PVDF	2387 ± 0.22	8.07 ± 0.000
DMF	HSV 1810	883 ± 0.07	24.08 ± 0.002
KJCMPA	PVDF	2054 ± 0.41	9.05 ± 0.002
KJCMPA	HSV 1810	1131 ± 0.08	16.50 ± 0.001

conductivity (17.72 S/m), while the remaining PVDF samples have conductivity below 10 S/m.

To identify the various phases of the binders dissolved in different solvents and blade coated, we initially employed XRD analysis, and its results are presented in Figure 10 and Figure S2. These results distinctly differentiate between PVDF and

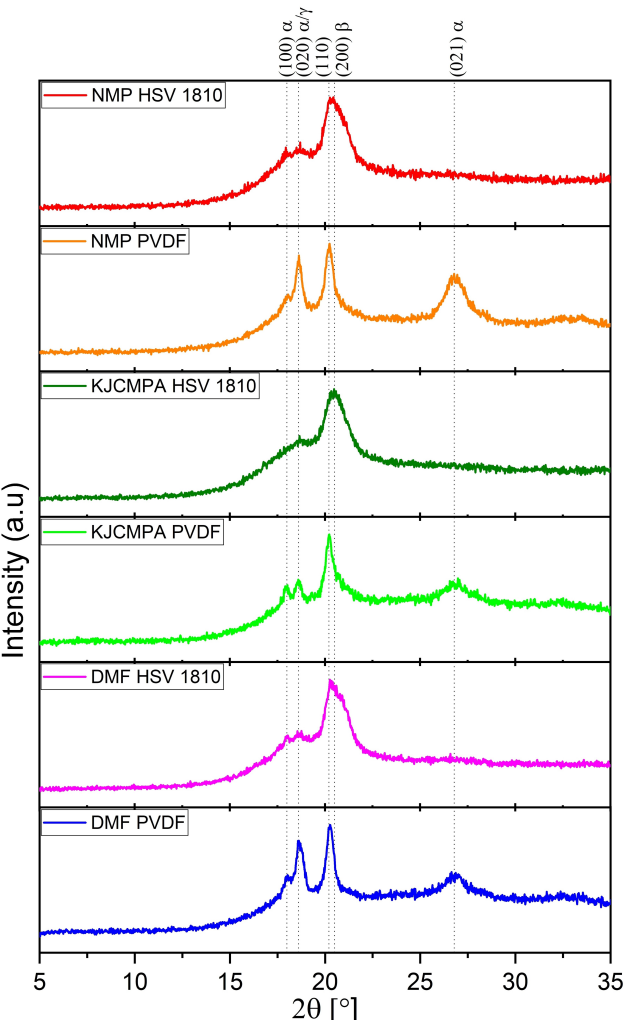


Figure 10. XRD analysis of solvent-binder films with highlighted peaks and their corresponding phases.

HSV 1810 films, regardless of the solvents used. Specifically, PVDF films indicate strong α -phase represented by peaks at 20 angles 27°, 18.4°, and 19°.

To verify and better understand the various phases, an FTIR analysis of the films has been conducted and the results are demonstrated in Figure 11. These findings align with the

previous XRD analysis. However, to quantify the different phases of the dissolved binder, a comprehensive method for distinguishing various phases in polymers solely through FTIR results developed by Cai et al. has been introduced.^[54] This approach distinguishes the α , β , and γ phases by examining bands near 763 and/or 614, 1275, and 1234 cm⁻¹, respectively. The results of this analysis are presented in Table 5.

The results reveal that all HSV 1810-based films predominantly exhibit a γ -phase: 65%, 12%, and 79% for NMP, DMF, and KJCMPA solvents, respectively. Also, all the HSV 1810-based films show low α -phase, while all PVDF-based films show over 60% of the α -phase in the binder films. The β -phase content in PVDF-based films varies between 34 and 39%. In HSV 1810-based films, β -phase is low for NMP (12%) and KJCMPA (0.2%), while for DMF, the β -phase represents over 53%.

After 1,000 cycles, we conducted a post-mortem SEM analysis of the cathodes, and provided the results in Supporting Figures (S3, S4, and S5). Our observations indicate that, when comparing pristine and cycled cathodes, the cathode structure remained largely unaltered for those fabricated with the NMP solvent, irrespective of the binder used. In contrast, cathodes made with DMF and KJCMPA solvents exhibited signs of degradation changes. Moreover, for the DMF solvent, when a HSV 1810 was utilized, the cycled cathodes appeared less disintegrated. However, cathodes fabricated with KJCMPA exhibited a consistent degree of disintegration, independent of the binder used. This finding corresponds with the results from SEM image analysis (Figure 6), which revealed visible cracks and irregularities, particularly in KJCMPA cathodes with a PVDF binder. Initially, these cells exhibit improved performance (likely due to enhanced electrolyte penetration), but prolonged cycling leads to accelerated degradation of KJCMPA-based cells. The presence of the cracks is consistent with surface conductivity measurements, which show that DMF- and KJCMPA-based cells have higher resistance compared to those based on NMP, which are crack-free. Increased viscosity of KJCMPA-based slurries might affect the quality of the films. However, the screen printer is capable of handling such viscous slurries and can still produce high-quality layers. Additionally, drying conditions are unlikely to be the root cause of the cracks, given that NMP and KJCMPA have similar boiling points.

Although the selected solvents and binders demonstrate excellent solubility, and the printed cathodes offer promising adhesion and film quality (visible to the naked eye), further research is essential. It is particularly important to understand the causes of crack formation in KJCMPA cathode films and to explore methods to mitigate this issue. Additionally, more research is required to comprehend the effects of novel solvents on the induction of various crystalline phases in cathode binders.

Conclusions

This study provides valuable insights into the complex interplay of solvents and binders in battery cathode fabrication. The

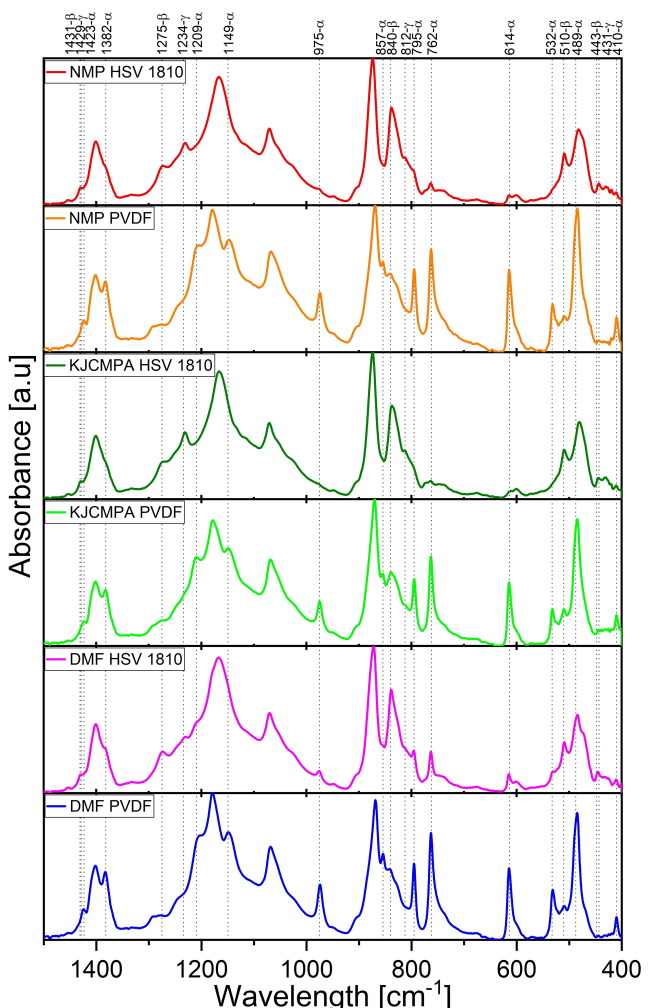


Figure 11. FTIR analysis of various solvent-binder films with highlighted peaks that indicate crystallinity phases.

Table 5. Calculated values of α -, β -, and γ -phases from the FTIR data acquired from the casted binders dissolved in various solvents.

Solvent	Binder	α -phase [%]	$\beta + \gamma$ [%]	β -phase [%]	γ -phase [%]
NMP	PVDF	62.63	37.63	37.63	0
NMP	HSV 1810	22.82	77.17	12.05	65.11
DMF	PVDF	65.60	34.39	34.39	0
DMF	HSV 1810	33.95	66.04	53.80	12.23
KJCMPA	PVDF	60.51	39.48	39.48	0
KJCMPA	HSV 1810	20.38	79.61	0.28	79.33

results indicate that the combination of NMP solvent with HSV 1810 binder exhibited superior performance in terms of cycling stability and capacity retention. The polarity of solvents significantly influenced their compatibility with binders, with polar solvents showing better synergy with PVDF-based binders. Electrochemical analyses revealed that HSV 1810 binders, especially when combined with NMP, demonstrated efficient electron transfer and superior cycling performance. Post-mortem SEM analysis after 1,000 cycles revealed that cathodes fabricated with NMP solvent maintained their structural integrity, irrespective of the binder used. In contrast, cathodes made with DMF and KJCPMA solvents showed noticeable degradation. While the environmental concerns associated with certain solvents, such as NMP, underscored the need for sustainable alternatives, the current options present challenges in terms of compatibility and performance. The research also highlighted the potential of printing techniques over traditional slot-die coating, emphasizing their adaptability and efficiency for modern battery designs. The findings pave the way for the development of more efficient and high-performing batteries, catering to the ever-growing demands of modern electronic devices, electric vehicles, and large-scale energy storage systems.

Methods

Prescreening – Solvents and Binders' Selection

In the first stage, a broad range of solvents and binders was examined. The solvents used included DMF, NMP, p-Xylene, Toluene, Cyrene (all from Merck KGaA), and KJCPMA-100 (KJ Chemicals Corp.). The binders employed were KF PVDF #9300, KF PVDF #1100 (both from Kureha Corp.), PVDF Kynar HSV 1810 (Arkema), PVP40 (Merck KGaA), Oppanol N150, and Oppanol B15 (both from BASF). Figure 2 displays the solvability behavior of these solvents and binders, and their influence on cathode adhesion to current collector.

Binders were combined with solvents in a ratio of 1 g/ml and stirred for 12 hours at room temperature. Subsequently, the solubility of each mixture was assessed. If a mixture produced a homogeneous suspension/solution, it was then utilized in adhesion tests. During these tests, the solvent-binder mixture was mixed with cathode active material/C45 and blade-coated onto the surface of a solvent-cleaned aluminum foil (current collector) to create an approximately 55 µm thick film (after drying). This film was dried on a hotplate at 100 °C for 1 hour. Post-drying, the films underwent optical analysis, and their adhesive properties were assessed using a tape-test method. Subsequent analyses, including slurry formulation, screen-printing, and battery assembly, incorporated only those mixtures that exhibited superior solubility and adhesive properties (Figure 2). The six solvent-binder combinations selected for further processing included NMP-PVDF #1100, NMP-HSV 1810, DMF-PVDF #1100, DMF-HSV 1810, KJCPMA-PVDF #1100, and KJCPMA-HSV 1810 (Figure 3).

Cathode Slurry Formulation

The experiment commenced with the formulation of cathode slurries. Lithium-Nickel-Manganese-Cobalt-Oxide ($\text{LiNi}_{0.5}\text{Mn}_{0.3}\text{Co}_{0.2}\text{O}_2$), was employed as the active material owing

to its proven stability and performance, as validated by numerous researchers. Commercial-grade NMC powders were procured from Targray, without the application of any supplementary treatment prior to usage. In the initial stage, the chosen solvent-binder mixtures were created by stirring the binder in the solvent for a duration of 12 hours at room temperature. Following this, the NMC active material was mixed with carbon black (C45) through a vortexing process that lasted for 3 minutes. Subsequently, the mixture of active material and carbon black was gradually added to the solvent-binder mix and stirred for an additional 6 hours. The slurries were formulated with a weight ratio of 92:4:4, comprising the active material, C45, and the binder. It was noted that the solvent and binder types significantly influenced the slurry's viscosity, the dispersion of NMC particles, and the binding strength. Slurry viscosity is a key factor, impacting the ease of the ensuing printing process. While diverse solvent-binder mixtures yielded slurries with varying viscosities and surface tensions (notably in KJCPMA-based inks), the solid content ratios were consistently maintained across all inks for consistency of the experiment. Despite these variations, all inks met the screen-printing requirements. To attain the targeted cathode thickness of 55 µm, printing parameters such as table-stencil distance, printing squeegee pressure and speed were optimized for each mixture.

Cathode Printing

The printing trials were conducted using an Ekra E2 screen printer with a Koenen stencil (VA 165–0.05 mm, W-Øx22.5°). To prevent any unintended solvent-squeegee interactions, particularly squeegee softening, a metal squeegee was employed for printing on the 20 µm-thick aluminum foil that served the purpose of a current collector. The temperature during printing was kept constant (23 °C) to ensure consistent slurry parameters.^[55] For each solvent-binder composition, three cathodes measuring 44x61 mm were printed at a speed varying between 30 and 60 mm/s, with a table-stencil gap of 0.5 to 2.0 mm, and a pressure range of 0.4 to 1.5 bar. Following the printing process, the cathodes underwent a drying process on a hotplate for 1 hour. This was necessary to remove any solvent residues and solidify the electrode material. Upon the completion of the drying process, these cathodes were utilized for both characterization and battery assembly. Samples selected for battery assembly were calendered three consecutive times (MTI Hot Rolls Press HR-02). The mass loading was approximately 12 ± 1.2 mg/cm².

Battery Assembly and Electrochemical Characterization

Pouch Cells: pouch cells, measuring 44x61 mm, were prepared for each sample composition. This included a graphite anode from Hitachi, an electrolyte of 1.15 M LiPF₆ in EC:DMC:EMC (2:4:4), and 1% vinylene carbonate. As separator, glass fiber (Advantec GA-100) was utilized. Following the formation cycles, these pouch cells underwent charging at a constant current of 1 C until reaching 4.2 V. This was succeeded by a constant voltage charge until the current dropped to 0.03 C. Discharging was conducted to 2.5 V at 1 C. All cells were tested at 25 °C. Additionally, capacity check cycles (0.2 C/0.2 C) were conducted every 100 cycles, but for the sake of clarity in the plotted figures, these checks were not represented. The theoretical capacities used to calculate the C-rate was 150 mAh/g. The pouch cells were balanced utilizing specific capacities: 150 mAh/g for NMC532 and 372 mAh/g for graphite. The balancing was performed such that the anode capacity surpassed the cathode capacity by an approximate 10%±2% margin. The assembly of all the batteries was performed in a dry

room kept at 25 °C, and the cycling process was facilitated using the MacCor Series 4000 battery cycler, and the results are presented in Figure 7 and Table 3.

Coin Cells: 2016-type coin cells were assembled for each sample cathode. Metallic lithium served as the counter electrode, while an electrolyte of 1 M LiPF₆ from Novolyte Technologies was used in combination with a 1:1:1 mixture of ethylene carbonate (anhydrous 99%, Sigma-Aldrich), diethyl carbonate (anhydrous 99%, Sigma-Aldrich), and dimethyl carbonate (\geq 99%, Novolyte Technologies), sealed under nitrogen. As separator, glass fiber (Advantec GA-100) was utilized. Initial charging was conducted at a constant current of 0.1 C until reaching a cut-off voltage of 4.3 V. Subsequently, a constant voltage was applied until the current reduced to 0.015 C during the first two cycles. For later cycles, the charging process remained the same, but with a current threshold increased to 0.02 C. Discharge during the first two cycles occurred at a constant current of 0.1 C until 2.6 V was met, followed by a constant voltage discharge until the current reached 0.015 C. A rate test involved an additional discharge to 3.0 V at varying C-rates. All tests were conducted at 25 °C and the results are presented in Figure 8.

Physicochemical Analysis

An examination of the formation and behavior of the cathode layers was conducted through a physicochemical analysis of two distinct types of samples. The first type consisted of six cathodes, screen-printed onto an aluminum current collector during printing trials. The second type, focused on binder phase analysis, involved six different solvent-binder compositions, each individually cast onto a glass substrate. This supplementary set of cast samples was specifically generated to exclude any potential interference from NMC and C45 materials in the results, a factor that was particularly significant during the FTIR and XRD analyses. The scanning electron microscopy (SEM) images (Figure 5 and 6) of the printed NMC films were performed using the JEOL JCM-5000 NeoScope at magnification 1,000. The post-mortem samples (Figures S3, S4, S5) were analyzed with Electron Microscope Zeiss ULTRA plus FESEM.

The EIS analysis (Figure 9) was conducted using an Arbin LBT21084UC battery testing system equipped with Gamry Instruments Interface 1010E extension. The characterization was performed at pouch cell batteries at frequency ranging from 2 MHz to 10 mHz. The modeling of equivalent circuit fit was conducted with a Gamry Echem analyst.

The viscosity of the samples was measured at room temperature using a Brookfield Viscometer DV-II+Pro EXTRA (model LVDV-II+PX). This measurement utilized the Rheocalc software provided by the manufacturer. Spindle 64 was consistently used for each measurement, ensuring uniformity. The results were recorded once the readings stabilized. The contact angle measurements were conducted immediately after the droplet formation on the glass substrate, utilizing a Kruss DSA100 system in a room temperature. The surface morphology of the printed cathodes was examined using a Bruker ConturGT optical profilometer.

The investigation into the crystalline structure of the phases present in the NMC cathodes (as printed (Figure S2a)) and after cycling (post-mortem (Figure S2b)) and six additional solvent-binder cast films (Figure 10) was carried out using X-ray powder diffraction (XRD) measurements at ambient temperature. The equipment used for this purpose was a Pananalytical instrument, specifically the X'pert 3 MRD model, which was operated at 45 kV and 40 mA. The detector used was an image plate type, and Cu-K α radiation K α 1 = 1.54 Å. The measurement protocol involved a scan rate of 0.0167°/min within the range of 10°–80° (20) and a step rate of 0.017° 2θ/step. The subsequent identification of phases and Rietveld refinement were accomplished utilizing the PDXL V.2 software (Rigaku, Japan) and a PDF-4+ 2020 database.

The FTIR characterization was conducted with a ThermoFisher Nicolet iS5 FTIR spectrophotometer in a range 4000–400 cm⁻¹, in ATR mode with a diamond crystal and the results are presented in Figure 11. These results were used to calculate the crystallinity of the used binders in respect to the utilized solvents. We utilized a method provided by Cai et al, and some of the details of this method are provided below.^[54]

The band at 840 cm⁻¹ can be attributed to either the β phase, the γ phase, or both, depending on additional band data. When considering the crystalline components in samples, the proportion of the electroactive β and γ phases (represented as F_{EA}) can be determined using the following equation (Eq. 1) for samples with either two phases (like $\alpha + \beta$, $\alpha + \gamma$, or $\beta + \gamma$) or three phases ($\alpha + \beta + \gamma$):

$$F_{EA} = \frac{I_{EA}}{\left(\frac{K_{840}}{K_{763}} \right) \cdot I_{763} + I_{EA}} \times 100\% \quad \text{Eq. 1}$$

In this equation, I_{EA} and I₇₆₃ denote the absorbances at 840 cm⁻¹ and 763 cm⁻¹, respectively, while K₈₄₀ and K₇₆₃ are the absorption coefficients for their respective wavenumbers, with values of 7.7×10^4 cm²mol⁻¹ and 6.1×10^4 cm²mol⁻¹. To further distinguish between the β and γ phases, we adopted the method introduced by Cai et al. This method calculates the peak-to-valley height ratio (P2VHR) for the peaks near 1275 cm⁻¹ and 1234 cm⁻¹ and their closest valleys, as shown in equations 2 and 3:

$$F(\beta) = F_{EA} \times \left(\frac{\Delta H_{\beta'}}{\Delta H_{\beta'} + \Delta H_{\gamma'}} \right) \times 100\% \quad \text{Eq. 2}$$

$$F(\gamma) = F_{EA} \times \left(\frac{\Delta H_{\gamma'}}{\Delta H_{\beta'} + \Delta H_{\gamma'}} \right) \times 100\% \quad \text{Eq. 3}$$

where $\Delta H_{\beta'}$ and $\Delta H_{\gamma'}$ represent the height (or absorbance) differences between the peaks near 1275 cm⁻¹ and 1234 cm⁻¹ and their closest valleys at approximately 1260 cm⁻¹ and 1225 cm⁻¹, respectively.

Post-Mortem Analysis

Upon completion of cycling, we conducted a post-mortem analysis on the cells. We disassembled the cells within the glove box, extracting the cathodes for closer examination. Each cathode was thoroughly rinsed with dimethyl carbonate (DMC) to remove any residual electrolyte, followed by drying in a vacuum oven at 60 °C overnight. Lastly, we used an SEM to investigate any structural or morphological changes on the cycled cathodes, comparing these findings with observations from the pristine samples. The SEM images (S3, S4, and S5) are provided in the Supporting Information document.

Supporting information

The files consist of the following information:

- Averaged values of specific capacity for PVDF and HSV 1810 binders, accompanied by standard deviation (Figure S1).

- Detailed values of electrical parameters extracted from the EIS spectra (Table S1).
- XRD analysis of cathodes with various solvent-binder compositions for pristine cathodes as printed and after 1,000 cycles (Figure S2).
- Comparison of pristine (as printed) and post-mortem (cycled 1,000 times) NMP-based cathodes for PVDF and HSV 1810 binders (Figure S3).
- Comparison of pristine (as printed) and post-mortem (cycled 1,000 times) DMF-based cathodes for PVDF and HSV 1810 binders (Figure S4).
- Comparison of pristine (as printed) and post-mortem (cycled 1,000 times) KJCPMA-based cathodes for PVDF and HSV 1810 binders (Figure S5).
- Morphological analysis of the printed cathodes (Table S2 and Figure S6).

Acknowledgements

The authors acknowledge the help and support of Jessica Nuorala and Markus Väyrynen. This research was funded by the EU/Interreg Nord – Interregional cooperation project (Project SolBat, grant no. 20202885). The authors also express their gratitude for the financial support received from the Academy of Finland's FIRI funding (grant no. 320017), Business Finland R2B Funding (grant no. 7270/31/2022, and EU/Interreg Aurora (Project GreenBattery, grant no 20357605).

Conflict of Interests

The authors declare no conflict of interest.

Data Availability Statement

The data that support the findings of this study are available from the corresponding author upon reasonable request.

Keywords: Printing · Battery Cathode · Binder HSV 1810 · PVDF Crystallinity · Solvents NMP DMF KJCPMA

- [1] Q. Guo, W. Zeng, S. L. Liu, Y. Q. Li, J. Y. Xu, J. X. Wang, Y. Wang, *Rare Met.* **2021**, *40*, 290–308.
- [2] J. Xie, Y. C. Lu, *Nat. Commun.* **2020**, *11*, 1–4.
- [3] H. Cavers, P. Molaiyan, M. Abdollahifar, U. Lassi, A. Kwade, *Adv. Energy Mater.* **2022**, *12*, 2200147.
- [4] H. S. Santos, R. Sliz, H. Nguyen, S. Srivastava, D. Ramteke, T. Fabritius, U. Lassi, P. Kinnunen, *Mater. Des.* **2022**, *217*, 110599.
- [5] A. Manthiram, J. L. Lutkenhaus, Y. Fu, P. Bai, B. G. Kim, S. W. Lee, E. Okonkwo, R. M. Penner, *One Earth* **2022**, *5*, 203–206.
- [6] J. Piątek, S. Afyon, T. M. Budnyak, S. Budnyk, M. H. Siiponen, A. Slabon, *Adv. Energy Mater.* **2021**, *11*, 2003456.
- [7] Y. Lin, J. Välikangas, R. Sliz, P. Molaiyan, T. Hu, U. Lassi, *Materials* **2023**, *16*, 3116.
- [8] A. Manthiram, *Nat. Commun.* **2020**, *11*, 1–9.
- [9] J. Välikangas, P. Laine, T. Hu, P. Tynjälä, M. Selent, P. Molaiyan, K. Jürgen, U. Lassi, *Small* **2023**, 2305349.
- [10] N. H. Kwon, D. Mouck-Makanda, K. M. Fromm, *Batteries* **2018**, *4*, 50.
- [11] Y. Shi, L. Wen, S. Pei, M. Wu, F. Li, *J. Energy Chem.* **2019**, *30*, 19–26.
- [12] D. Miranda, A. Gören, C. M. Costa, M. M. Silva, A. M. Almeida, S. Lanceros-Méndez, *Energy* **2019**, *172*, 68–78.
- [13] X. Jiao, A. V. Kirianova, X. Xu, O. O. Kapitanova, V. A. Krivchenko, F. S. Napolkskiy, V. S. Volkov, M. O. Gallyamov, Y. Liu, *ACS Appl. Energ. Mater.* **2023**, *6*(5), 2855–2862.
- [14] K. Wang, Q. Ye, J. Zhang, H. Huang, Y. Gan, X. He, W. Zhang, *Front. Mater.* **2021**, *8*, 727617.
- [15] J. Yang, P. Li, F. Zhong, X. Feng, W. Chen, X. Ai, H. Yang, D. Xia, Y. Cao, *Adv. Energy Mater.* **2020**, *10*, 1904264.
- [16] H. Xu, K. Jiang, X. Zhang, X. Zhang, S. Guo, H. Zhou, *ACS Appl. Mater. Interfaces* **2019**, *11*, 26817–26823.
- [17] P. Li, J. Zhu, C. Wang, J. Wang, X. Yang, K. Zhang, Z. Shen, G. Qiu, F. Han, Y. Hou, *Electrochim. Acta* **2021**, *389*, 138784.
- [18] J. H. Teo, F. Strauss, F. Walther, Y. Ma, S. Payandeh, T. Scherer, M. Bianchini, J. Janek, T. Brezesinski, *Mater. Futures* **2022**, *1*, 015102.
- [19] T. Ates, M. Keller, J. Kulisch, T. Adermann, S. Passerini, *Energy Storage Mater.* **2019**, *17*, 204–210.
- [20] Z. Zhang, T. Zeng, Y. Lai, M. Jia, J. Li, *J. Power Sources* **2014**, *247*, 1–8.
- [21] S. H. Sung, S. Kim, J. H. Park, J. D. Park, K. H. Ahn, *Materials* **2020**, *13*, 4544.
- [22] L. Yang, H. Wang, S. Fang, M. Li, *J. Alloys Compd.* **2023**, *960*, 170831.
- [23] P. Martins, A. C. Lopes, S. Lanceros-Mendez, *Prog. Polym. Sci.* **2014**, *39*, 683–706.
- [24] M. Yuan, H. Wang, T. Wang, H. Yang, C. Yuan, *ACS Appl. Polym. Mater.* **2023**, *5*, 2664–2673.
- [25] N. Zhu, J. Zhou, L. Zhang, N. Yao, D. Dastan, J. Zhang, Y. Chen, X. Zhang, *Soft Matter* **2023**, *19*, 4401–4431.
- [26] T. Song, Y. Wang, H. Li, H. Wang, X. Sun, S. Yan, *Macromolecules* **2022**, *55*, 10912–10920.
- [27] Y. Zhao, W. Yang, Y. Zhou, Y. Chen, X. Cao, Y. Yang, J. Xu, Y. Jiang, *J. Mater. Sci. Mater. Electron.* **2016**, *27*, 7280–7286.
- [28] W. Li, Q. Meng, Y. Zheng, Z. Zhang, W. Xia, Z. Xu, *Appl. Phys. Lett.* **2010**, *96*, DOI 10.1063/1.3428656/120116.
- [29] T. Song, Y. Wang, H. Li, H. Wang, X. Sun, S. Yan, *Macromolecules* **2022**, *55*, 10912–10920.
- [30] W. J. Song, S. H. Joo, D. H. Kim, C. Hwang, G. Y. Jung, S. Bae, Y. Son, J. Cho, H. K. Song, S. K. Kwak, S. Park, S. J. Kang, *Nano Energy* **2017**, *32*, 255–262.
- [31] M. M. Loghavi, S. Bahadorikhahili, N. Lari, M. H. Moghim, M. Babaee, R. Eqra, *Z. Phys. Chem.* **2020**, *234*, 381–397.
- [32] Y. Ren, Y. Wang, W. Zhang, X. Yan, B. Huang, *RSC Adv.* **2019**, *9*, 29760–29764.
- [33] M. Kundu, C. M. Costa, J. Dias, A. Maceiras, J. L. Vilas, S. Lanceros-Méndez, *J. Phys. Chem. C* **2017**, *121*, 26216–26225.
- [34] E. Lizundia, A. Reizabal, C. M. Costa, A. Maceiras, S. Lanceros-Méndez, *Materials* **2020**, *13*, 743.
- [35] J. Luo, C.-C. Fang, N.-L. Wu, J. Luo, N.-L. Wu, C.-C. Fang, *Adv. Energy Mater.* **2018**, *8*, 1701482.
- [36] R. Sliz, J. Valikangas, H. Silva Santos, P. Vilmi, L. Rieppo, T. Hu, U. Lassi, T. Fabritius, *ACS Appl. Energ. Mater.* **2022**, *5*, 4047–4058.
- [37] F. Gao, R. Bai, F. Ferlin, L. Vaccaro, M. Li, Y. Gu, *Green Chem.* **2020**, *22*, 6240–6257.
- [38] R. Sliz, J. Valikangas, P. Vilmi, T. Hu, U. Lassi, T. Fabritius, *2021 IEEE 16th Nanotechnology Materials and Devices Conference, NMDC 2021*.
- [39] A. Jordan, C. G. J. Hall, L. R. Thorp, H. F. Sneddon, *Chem. Rev.* **2022**, *122*, 6749–6794.
- [40] M. Wood, J. Li, R. E. Ruther, Z. Du, E. C. Self, H. M. Meyer, C. Daniel, I. Belharouak, D. L. Wood, *Energy Storage Mater.* **2020**, *24*, 188–197.
- [41] M. Bichon, D. Sotta, N. Dupré, E. De Vito, A. Boulineau, W. Porcher, B. Lestriez, *ACS Appl. Mater. Interfaces* **2019**, *11*, 18331–18341.
- [42] W. B. Hawley, A. Parejiya, Y. Bai, H. M. Meyer, D. L. Wood, J. Li, *J. Power Sources* **2020**, *466*, 228315.
- [43] G. Yang, M. Zhang, I. Majeed, W. Fan, J. Zhao, Z. Zeng, *ACS Sustainable Chem. Eng.* **2023**, *11*, 14582–14590.
- [44] N. Phattharasupakun, J. Wutthiprom, S. Duangdangchote, S. Sarawutanukul, C. Tomon, F. Duriyasart, S. Tubtimkuna, C. Aphirakaramwong, M. Sawangphruk, *Energy Storage Mater.* **2021**, *36*, 485–495.
- [45] M. Ryu, Y. K. Hong, S. Y. Lee, J. H. Park, *Nat. Commun.* **2023**, *14*, 1–10.
- [46] L. J. Deiner, T. Jenkins, T. Howell, M. Rottmayer, *Adv. Eng. Mater.* **2019**, *21*, 1900952.
- [47] R. Gonçalves, P. Dias, L. Hilliou, P. Costa, M. M. Silva, C. M. Costa, S. Corona-Galván, S. Lanceros-Méndez, *Energy Technol.* **2021**, *9*, 2000805.

- [48] R. Sliz, E. Hannila, I. S. Roy, J. Valikangas, P. Molaiyan, U. Lassi, T. Fabritius, 2023 IEEE 23rd International Conference on Nanotechnology, NANO **2023**, 363–366.
- [49] C. M. Costa, R. Gonçalves, S. Lanceros-Méndez, *Energy Storage Mater.* **2020**, 28, 216–234.
- [50] R. Sliz, P. Molaiyan, T. Fabritius, U. Lassi, *Nano express* **2022**, 3, 021002.
- [51] U. Westerhoff, K. Kurbach, F. Liemesch, M. Kurrat, *Energy Technol.* **2016**, 4, 1620–1630.
- [52] J. Schmalstieg, C. Rahe, M. Ecker, D. U. Sauer, *J. Electrochem. Soc.* **2018**, 165, A3799–A3810.
- [53] H. Beltran, P. Ayuso, N. Vicente, B. Beltrán-Pitarch, J. García-Cañadas, E. Pérez, *J. Energy Storage* **2022**, 52, 104747.
- [54] X. Cai, T. Lei, D. Sun, L. Lin, *RSC Adv.* **2017**, 7, 15382–15389.
- [55] R. Sliz, Y. Suzuki, T. Fabritius, R. Myllyla, *Colloids Surf. A* **2014**, 443, 182–187.

Manuscript received: November 10, 2023

Revised manuscript received: January 4, 2024

Accepted manuscript online: January 11, 2024

Version of record online: January 25, 2024
